Nanoscale Advances

ROYAL SOCIETY OF CHEMISTRY

PAPER

View Article Online
View Journal | View Issue

Cite this: *Nanoscale Adv.*, 2024, **6**, 1202

Vortex fluidic regulated phospholipid equilibria involving liposomes down to sub-micelle size assemblies†

Nikita Joseph,‡[a] Marzieh Mirzamani,‡[b] Tarfah Abudiyah,[a] Ahmed Hussein Mohammed Al-Antaki,[ac] Matt Jellicoe,[a] David P. Harvey,[a] Emily Crawley,[a] Clarence Chuah,[a] Andrew E. Whitten,[d] Elliot Paul Gilbert,[d] Shuo Qian,[e] Lilin He,[f] Michael Z. Michael,[g] Harshita Kumari *[b] and Colin L. Raston *[a]

Conventional channel-based microfluidic platforms have gained prominence in controlling the bottom-up formation of phospholipid based nanostructures including liposomes. However, there are challenges in the production of liposomes from rapidly scalable processes. These have been overcome using a vortex fluidic device (VFD), which is a thin film microfluidic platform rather than channel-based, affording ~110 nm diameter liposomes. The high yielding and high throughput continuous flow process has a 45° tilted rapidly rotating glass tube with an inner hydrophobic surface. Processing is also possible in the confined mode of operation which is effective for labelling pre-VFD-prepared liposomes with fluorophore tags for subsequent mechanistic studies on the fate of liposomes under shear stress in the VFD. *In situ* small-angle neutron scattering (SANS) established the co-existence of liposomes ~110 nm with small rafts, micelles, distorted micelles, or sub-micelle size assemblies of phospholipid, for increasing rotation speeds. The equilibria between these smaller entities and ~110 nm liposomes for a specific rotational speed of the tube is consistent with the spatial arrangement and dimensionality of topological fluid flow regimes in the VFD. The prevalence for the formation of ~110 nm diameter liposomes establishes that this is typically the most stable structure from the bottom-up self-assembly of the phospholipid and is in accord with dimensions of exosomes.

Received 6th December 2023
Accepted 17th January 2024

DOI: 10.1039/d3na01080e

rsc.li/nanoscale-advances

Introduction

Liposomes are composed of self-assembled bilayers of phospholipid which confine space, segregating the inner compartment from an aqueous surrounding environment. They have emerged as vehicles for drug and gene delivery applications, which relate to the liposomes mimicking cell behaviour and enabling their protection from the immune responses of the body.[1,2] They are not only of interest in simulating the size and function of exosomes[3,4] but are also used as bio-analytical tools, as in immunoassays, biosensors and liposome-nanotube networks.[1,2] These lipid assemblies can be altered and manipulated in specific carrier systems for developing novel approaches towards clinical and analytical applications.[5,6]

Fabricating liposomes using conventional methods involves a number of critical steps, including dissolving lipid molecules in a suitable solvent, solvent evaporation for producing a thin film and extracting liposomes by hydrating the thin film on the addition of different solvents.[5] This complex processing was given a new direction using channel-based microfluidic platforms. Such microfluidic systems can result in high response to controlling the properties of the liposomes in terms of size, distribution, lamellar order and polydispersity.[5–11] Transforming this technology to clinical scale processing raises a number of challenges in addressing the viability of generating liposomes on the macro-scale where the processing is diffusion controlled under laminar flow, with low Reynolds numbers.[5,11]

[a]*Flinders Institute for Nanoscale Science and Technology, College of Science and Engineering, Flinders University, Bedford Park, SA 5042, Australia. E-mail: colin.raston@flinders.edu.au*

[b]*James L. Winkle College of Pharmacy, University of Cincinnati, Cincinnati, OH 45267-0004, USA. E-mail: kumariha@ucmail.uc.edu*

[c]*Department of Chemistry, Faculty of Science, University of Kufa, Najaf 54001, Iraq*

[d]*Australian Nuclear Science and Technology Organisation (ANSTO), Lucas Heights, NSW 2234, Australia*

[e]*The Second Target Station Project of SNS, Oak Ridge National Laboratory, Oak Ridge, TN 37830, USA*

[f]*Neutron Scattering Division, Oak Ridge National Laboratory, Oak Ridge, TN 37830, USA*

[g]*Flinders Centre for Innovation in Cancer (FCIC), Flinders Medical Centre (FMC), Bedford Park, SA 5042, Australia*

† Electronic supplementary information (ESI) available. See DOI: https://doi.org/10.1039/d3na01080e

‡ Authors contributed equally to this work.

These challenges include complex time consuming operations, limited reproducibility, and scaling up. They arise from restrictions associated with the prevailing focus of the microfluidic hydrodynamic approach (MHF), as a lab-on-a-chip device,[5] with recent advances in overcoming them using a microfluidic mixing device,[11] with future prospects on using machine learning in the microfluidic processing.[12] An alternative approach is using the recently developed thin film microfluidic platform, the vortex fluidic device (VFD), Fig. 1;[14–26] in this case, film thickness is typically less than 500 μm, falling within the realms of microfluidics. The VFD has a rapidly rotating tube open at one end, and at high rotational speed, shear stress is generated producing thin films of different thickness, depending on the orientation and rotational speed of the tube. The associated dynamic thin films are pivotal for applications of the device in chemical and materials transformations.[13–16]

The VFD can be operated in the confined mode, where a finite amount of liquid is allowed to undergo processing for a specific time, or continuous flow mode for scaling up the process.[9] For the latter, the liquid is continuously delivered into the rapidly rotating tube at different flow rates and rotational speeds, *via* syringe pumps or similar equipment, and the product is collected at the other end. In addition, sequential processing can be done by connecting the out flow from one VFD to another VFD.[14] The VFD has a diverse range of applications including modulating protein folding,[17] accelerating enzymatic reactions,[15] controlling chemical selectivity and reactivity,[18,19] tuning hydrogel properties,[20] manipulating the surfactant and interface for functional food structure and encapsulation,[21,22] fabricating porous spheres of cross linked BSA protein with glutaraldehyde and[23] and also monitoring real-time bio-sensing applications.[24] The optimal operating parameters for any application depend on the rotational speed (ω) of the hemispherical based tube and its tilt angle (θ) relative to the horizontal position, which is usually +45° noting that it also can take on a negative value, and the signature of the liquid.[25] The latter is defined as the impact of rotational speed on mixing times for a drop of liquid to mix halfway up the tube, change in temperature monitored midway along the tube, and the average film thickness.[25] The thin film fluid has high Reynolds numbers with different high shear stress topological fluid flows down to sub-micron dimensions, Fig. 1.[25,26] They are the spinning top (typhoon like) flow which is a Coriolis force from the hemispherical base of the tube, and double helical flow as eddies generated by Faraday waves.[25,26]

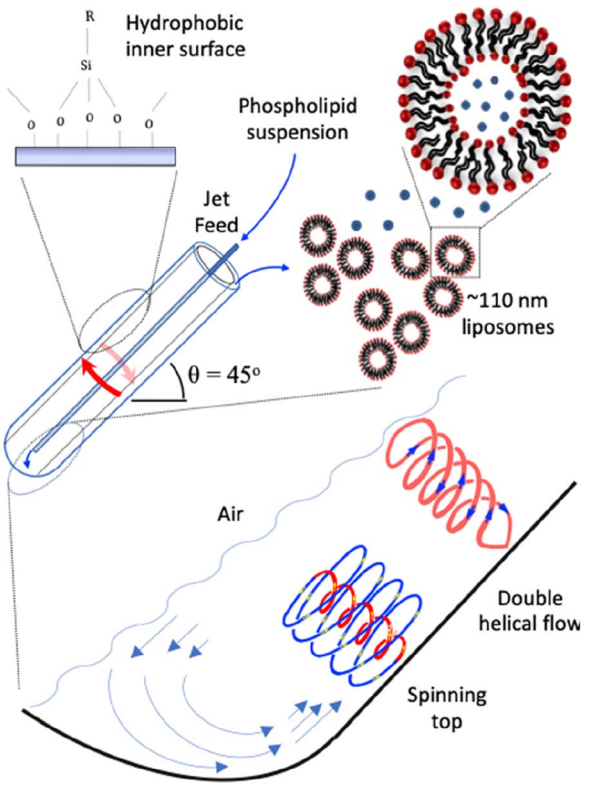

Fig. 1 Schematic representation of the vortex fluidic device (VFD) and high shear topological spinning top (typhoon like) and double helical fluid flows.[25,26] The phospholipid suspension is passed to the bottom of the tube through one jet feed at a specific concentration, varied from 25 μg mL^{-1} to 0.1 mg mL^{-1} in 25 μg increments, and then 0.5, 0.75 and 1.0 mg mL^{-1}, ω 9000 rpm, θ +45°, and under continuous flow at 0.1 mL min^{-1}, in a 20 mm (O.D.) hydrophobic tube. The collected liposomes are uni-lamellar ~110 nm in diameter.

We report herein the processing of liposomes at a macroscale with the formation of ~110 nm liposomes in water across the rotation landscape when θ is +45°. Moreover, we establish the ability to prepare fluorophore labelled liposomes based on the same phospholipids in the VFD, depending on its operating parameters, in particular for low rotational speeds. We hypothesised that these fluid flows would be effective in reorganising phospholipids into different structures through shear stress disassembly and which would subsequently reassemble, at some distance away from the topological fluid flows, to the thermodynamically favoured structure. Formation of the liposomes occurs at lower phospholipid concentrations relative to that used in conventional batch processes[5] as the critical micelle concentration is reached much faster in the VFD due to high mass transfer under controlled topological shear stress.[25,26] This bottom-up control of self-assembly in forming liposomes is a paradigm shift for rapid, high throughput and scalable processing for generating liposomes. Its simplicity is in contrast to the requirements of membrane extrusion to prepare liposomes.[5,6] The mechanism of VFD-mediated formation of liposomes has also been studied herein using *in situ* small-angle neutron scattering (SANS),[27] establishing the formation of small assembled arrays of phospholipids down to micelles and monomeric phospholipids which are in equilibrium with ~110 nm liposomes. We recently developed this *in situ* technique in the VFD for real time studies of encapsulation of fish oil.[27] Liposomes of this dimension represent the thermodynamically favoured bottom-up assembly of phospholipid molecules not experiencing shear stress topological fluid flows within the thin liquid film in the VFD, Fig. 2. Interestingly, the formation of ~110 nm liposomes matches the approximate size of exosomes.[3,4] Shear stresses in the thin film of liquid in the VFD can be localised rather than being uniform throughout.[25,26]

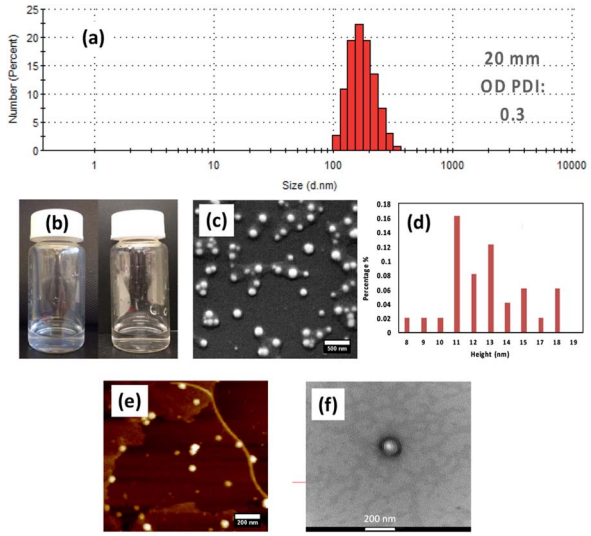

Fig. 2 (a) Dynamic light scattering (DLS) data – the highest number of particles at 200 nm with a polydispersity index (PDI) of 0.3. (b) Pre-VFD and post-VFD solutions for 1 mg mL^{-1} phospholipid (POPC) solution in Milli-Q water processed at ω 9000 rpm, flow rate 0.1 mL min^{-1} using a hydrophobic tube, θ +45°. (c) SEM image for VFD processed liposomes in (b), with the sample sputter coated with ~2 nm Pt deposition before imaging. Scale bar is 500 nm. (d) AFM height distribution profile for post-VFD processed liposomes as for (e), the sample being imaged with a fast scan assist peak force microscope in tapping mode on a silicon surface; scale bar is 200 nm. (f) TEM image for VFD processed liposomes as in (b) with the sample stained with 2% uranyl acetate and air dried on a copper grid before imaging. The voltage applied was 80–100 kV. Scale bar is 200 nm.

Shear stress induced aggregation of colloids[28] and colloidal breakup[29] may be understood at a theoretical level by accounting for flow-mediated transport of molecules.

Results and discussion

The optimal conditions for generating liposomes in the VFD under continuous flow were for a flow rate ($\dot{\nu}$) of 0.1 mL min^{-1} with the glass tube spun at ω of 9000 rpm at a tilt angle θ of +45° relative to the horizontal position, Fig. 1. This was established by systematically exploring the operating parameters of the device (see ESI Sections 3–6†), which includes, in addition to flow rate, rotational speed and title angle, the hydrophobicity of the inner surface of the tube as well as the concentration of the phospholipid; in the present case, this was POPC in Milli-Q water at specific concentrations, 50 μg mL^{-1} and 1 mg mL^{-1} *i.e.* 20× greater. Initially, the confined mode of operation of the VFD was used for process optimisation; for subsequent operation, the VFD was operated under continuous flow.[9] The tubes were borosilicate glass or quartz, 20 mm in diameter (~17.5 mm internal diameter), 18.5 cm in length, and with a hemispherical base. We found that the phospholipid covered the inner surface of the tube when using the confined mode. This build-up of phospholipid was circumvented by rendering the inner surface hydrophobic by coating with dodecylsilane (see ESI Section 2).†

Processed solutions (confined mode and continuous flow) were analysed using Nanoparticle Tracking Analysis (NTA), to provide particle size distribution. The mean diameter of the liposomes at the optimal conditions was ~110 nm, Fig. 2. The spheroidal shape of the particles was determined using scanning electron microscopy (SEM), transmission electron microscopy (TEM) and atomic force microscopy (AFM) (Fig. 2). SEM established that the particles are 100 to 200 nm in diameter which is consistent with results from TEM, and AFM as determined from the height profile.[30] The thickness of a phospholipid bilayer is 4.5 nm while that of a deflated uni-lamellar liposome is reported to be ~10 to 12 nm.[30] Given that the particles were sputter coated with ~2 nm of platinum, the average thickness of 15.9 nm, as determined from counting 100–200 particles, is closer to the formation of uni-lamellar liposomes. The assembly of POPC into liposomes is essentially quantitative, as judged from DLS, SEM and AFM data. Other assembly methods can give variable outcomes, including in controlling the size of the liposomes.[5–12] The overall stability of the liposomes will be largely independent of the method used to generate them.

The nature of the inner surface of the tube also affected the processing outcome in forming liposomes, beyond the POPC initially coating the surface of the tube when the surface is hydrophilic, thereby consuming/wasting the phospholipid before processing the POPC in the liquid. The hydrophobic tube avoids the formation of this coating, and indeed it improves the polydispersity index (PDI) obtained from dynamic light scattering (DLS) for liposomes formed under continuous flow in the VFD. The reason for the higher PDI for hydrophilic tubes, implying less control over the self-assembly process, is unclear. However, we note that the fluid flow in the VFD is complex under high shear associated with sub-micron topological fluid flows, Fig. 1,[25,26] and where mixing is down to nm dimensions and diffusion control is not a limiting factor. Nevertheless, it is more energetically favourable for the hydrophobic chain in a phospholipid to associate with other hydrophobic chains to minimise its surface area in aqueous environment, despite a resulting decrease in entropy. The arrangement of phospholipids with their hydrophilic head groups in contact with water lowers the interfacial tension but, in a hydrophilic tube, the expected drag of the polar head groups with the hydrophilic glass surface will perturb the fluid dynamics, and presumably this is at the expense of controlling the self-assembly process. This will be the case for the high shear spinning top topological fluid flow, Fig. 1, which is responsible for a number of applications of the VFD, for example in exfoliating 2D material such as graphene, phosphorene and MoS_2.[31] It should be noted that the choice of hydrophilic or hydrophobic tube is essentially another operating parameter of the VFD and an understanding on how this will impact on chemical reactions and self-assembly in the present study is the subject of ongoing studies.

The above results are for the 20 mm OD diameter VFD tube (~17.5 mm internal diameter); we subsequently studied the processing in smaller diameter tubes, 10 mm OD and 15 mm OD glass tubes, with the tubes similarly coated to render them hydrophobic. Studying different diameter tubes is possible

using interchangeable bearings in the standard 20 mm diameter VFD. For both smaller diameter tubes, the polydispersity is less controlled, and this is consistent with a greater range of particle height profiles when processing in these tubes, as determined from AFM studies, Fig. 3.

The self-assembly of phospholipids in dynamic thin films under high shear in the VFD is inherently complex, and *in situ* techniques can provide information on the mechanism of the liposome formation. To this end we explored the utility of *in situ* small-angle neutron scattering (SANS) for measuring the size and shape of phospholipid structures generated under shear on length scales spanning 1 to a few hundred nanometres. We recently developed this *in situ* VFD technique for real time nanoencapsulation.[27] Here, the influence of a hydrophobic coating on the inner surface of the VFD tube on the phospholipid interplay was also tested. Data were collected at ANSTO using a VFD tube with a hydrophobic coating on the inner surface, while data collected at ORNL[32] had no coating.

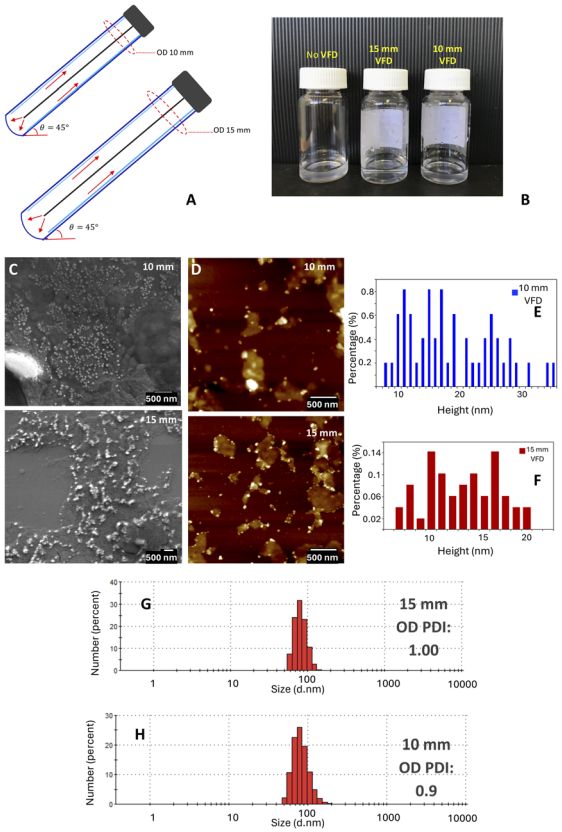

Fig. 3 (A) Schematic representation for hydrophobic coated VFD tube, 10 mm and 15 mm OD. (B) Pre-VFD and post VFD solutions processed at ω 9000 rpm in confined mode, concentration 1 mg mL^{-1}, tilt angle θ +45° in both tubes. (c) SEM image for VFD processed liposomes; the sample was sputter coated with 2 nm Pt deposition before imaging. Scale bar 500 nm. (D) AFM images and height distribution profile for VFD processed liposomes in 10 and 15 mm OD tubes; the sample were scanned with in tapping mode on a silicon surface. Scale bars 500 nm (E) and (F) AFM height thickness of the particles formed in 10 and 15 mm OD tubes respectively. (G) and (H) DLS distribution plots for particles formed in 10 and 15 mm OD tubes, respectively.

The SANS data and their fits using a summed, unsmeared power law + Lorentzian peak model are shown in Fig. 4. All data, regardless of the real-time or after shear and whether the tube had a hydrophobic coating, exhibited strong low-q scattering and a well-defined peak at $q \approx 0.1$ Å^{-1}. The low-q scattering is caused by structures with dimensions $\gg q_{min}^{-1}$, where q_{min} is the minimum accessible q value, and arises from vesicles, liposomes or similar 'large-scale' structures. The slope of the low-q scattering reflects the smoothness of the surface of these structures. The peak, on the other hand, is caused by the intraparticle repeat, which in this case would primarily be characteristic of multilamellar liposomes. These general features did not change as the shearing speed increased, indicating that there were no significant changes in what structures were present in the systems as a function of shear. However, some similarities between the *in situ* shear data from ANSTO and ORNL and differences between the *in situ* and post shear data from ANSTO could be identified. The real-time shear data from ANSTO and ORNL (Fig. 4d and f, respectively) both had slight excess scattering at $q = 0.04$ Å^{-1}, between the peak and the low-q scattering, that could suggest the presence of some small amount of POPC rods or vesicles. Comparing the real-time shear and post-shear data from ANSTO (Fig. 4d and e), the strength of the peak in the post-shear data was much weaker than it was in the real-time shear data, indicating that the systems had fewer multilamellar structures after being sheared, regardless of shear speed.

To better analyse the data, a number of models were fitted, with the power law + Lorentzian peak summed model ultimately being chosen for all data sets. Other summed models that were tested included, but were not limited to, power law + cylinder, power law + vesicle, and power law + multilamellar vesicle. Of these, the power law + multilamellar vesicle model provided visually reasonable fits but not as well as the chosen model. Table 1 summarises the fitting parameters for the real-time ANSTO data using the tube with a hydrophobic coating, Table 2 for the real-time ORNL data using the uncoated tube, and Table 3 for the post-shear ANSTO data. The power law exponent from the model fitting of the low q data provides information on the surface smoothness of the large structures where a value of 4 indicates a smooth surface and a value of 3 is the limit of roughness; the half-width half-maximum (HWHM) of the Bragg peak at high q relates to the variation in thickness of the multilamellar structure; the average thickness of the multilamellar structure can be determined from the position of the peak using the relation $d = 2\pi/q$; and the ratio of the scale factors between the power law and Bragg peak gives a relative measure of the amount of POPC present as multilamellar structures.[33]

The unsheared system collected at ANSTO (Table 1) acts as a baseline to determine how the POPC system responds to increasing shear both during and after shear. The unsheared sample was loaded into a Hellma 120-QS 2 mm quartz cell and can be compared to the *in situ* data collected at ANSTO. Before shear, the surface of the large structures are moderately rough, the multilamellar structures are approximately 64.4 Å thick, and the POPC is predominantly located in the multilamellar structures as indicated by the small power scale : peak scale ratio.

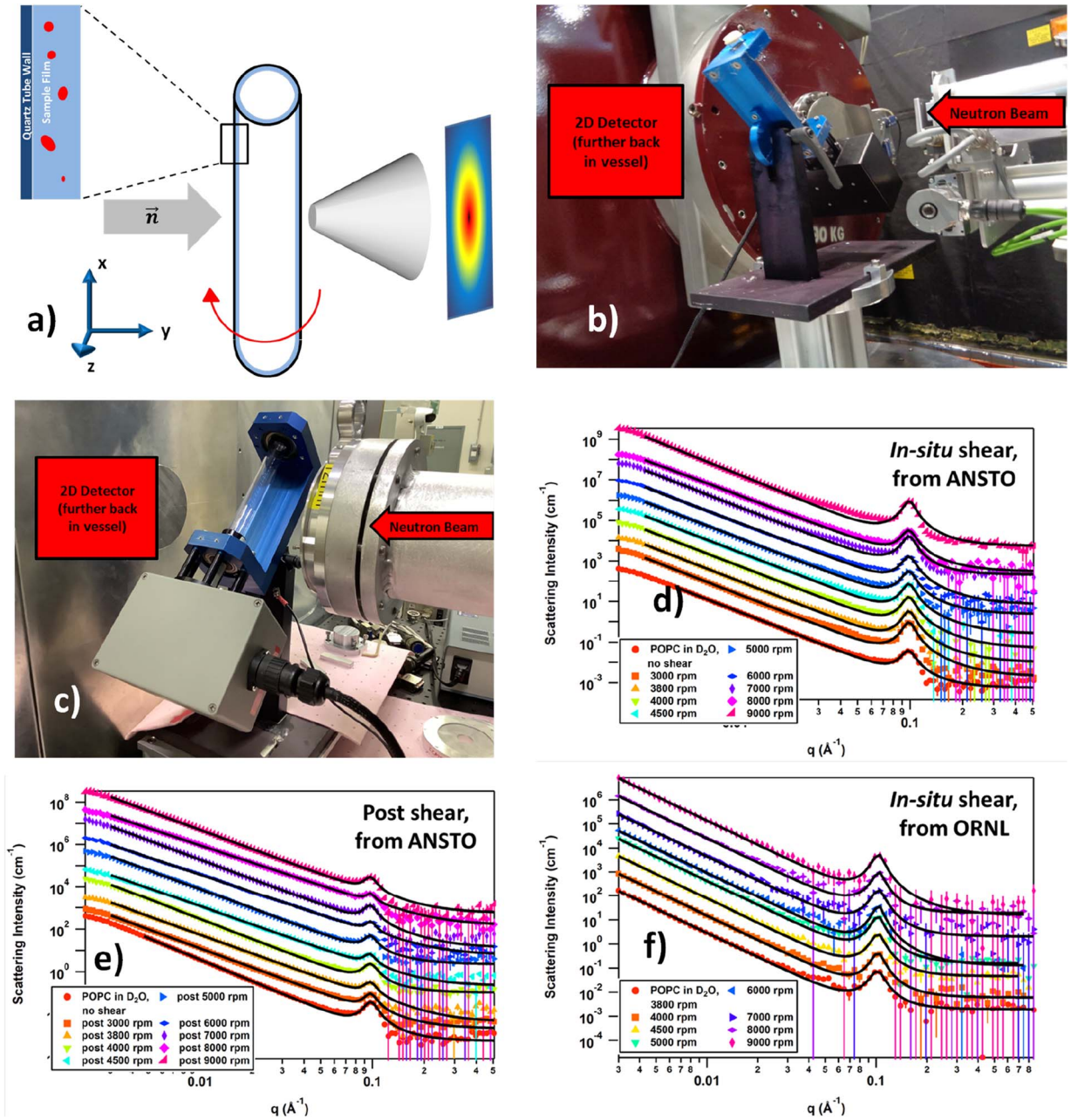

Fig. 4 SANS data overlays of POPC liposomes in D_2O at each shear level generated at the specified rotational speeds: (a) overhead-view schematic of the VFD tube, the sample film, and the neutron beam passing through and being scattered by the tube and sample film before meeting the 2D-detector; (b) BILBY sample area at ANSTO including the VFD setup; (c) Bio-SANS sample area at ORNL including the VFD setup; (d) real-time VFD-SANS data collected from ANSTO as a function of increasing rotational speeds; (e) static SANS measurements collected from ANSTO after each real-time VFD study; (f) real-time VFD-SANS data collected on the Bio-SANS instrument at ORNL. Each data set in (d)–(f) were offset by powers of 5 for clarity, and the black lines are the model fits to the data using a power law + Lorentzian peak summed model. Data collected at ANSTO utilized a quartz tube that had a hydrophobic coating on the inner surface; in contrast, the quartz tube used for the ORNL data collection had no coating to enable comparison of the results.

Once the system is subjected to shear in the hydrophobically coated tube, slight changes become apparent: the slope of the low-q scattering decreases, the peak initially becomes narrower as the speed of rotation increases, but does appear to broaden again at high speed. The d-spacing shrinks as rotational speed increases, and the power scale : peak scale ratio decreases when the system is under shear, then trends upwards with speed. These changes overall suggest that shear induces the POPC to move from the surface of the large liposomes to either the multilamellar structures, the bulk solution as free monomer, or formation of unilamellar liposomes, causing the surface roughness to increase and the concentration of POPC in the large liposomes to decrease.

Table 1 SANS fits for the real-time VFD-SANS data at increasing VFD speeds, at ANSTO using a quartz tube with a hydrophobic coating on the inner surface. The 0 rpm/unsheared sample was not sheared so any changes in structure due to shear in the VFD could be identified. The data were fitted with a summed power law + Lorentzian peak model. The peak HWHM indicates the width of the peak. The *d*-spacing was calculated from the peak position determined by the Lorentzian peak model, using the equation $d = 2\pi/q$, where q is the scattering vector. The ratio of the power scale to the peak scale indicates how much of the POPC is held in large structures like vesicles or liposomes *versus* the amount of POPC in multilamellar structures. Smaller ratios mean more POPC is in multilamellar structures. The digit in parentheses is the error in the last significant figure, and was calculated with either error propagation or from the SANS fit

Real-time VFD speed	(−) Power	Peak HWHM	*d*-spacing (Å)	Power scale/peak scale ratio
0 rpm (unsheared)	3.367(2)	$8.4(1) \times 10^{-3}$	64.39(5)	$1.85(2) \times 10^{-5}$
3000 rpm	3.360(2)	$6.91(5) \times 10^{-3}$	63.97(2)	$5.27(6) \times 10^{-6}$
3800 rpm	3.346(3)	$7.05(7) \times 10^{-3}$	63.91(3)	$7.4(1) \times 10^{-6}$
4000 rpm	3.325(2)	$7.25(6) \times 10^{-3}$	63.96(3)	$8.9(1) \times 10^{-6}$
4500 rpm	3.318(2)	$7.30(8) \times 10^{-3}$	63.98(3)	$1.02(1) \times 10^{-5}$
5000 rpm	3.300(2)	$7.7(1) \times 10^{-3}$	64.07(4)	$1.32(2) \times 10^{-5}$
6000 rpm	3.264(2)	$7.7(1) \times 10^{-3}$	63.99(4)	$1.59(2) \times 10^{-5}$
7000 rpm	3.343(2)	$7.39(6) \times 10^{-3}$	63.82(2)	$6.73(7) \times 10^{-6}$
8000 rpm	3.214(2)	$8.0(2) \times 10^{-3}$	64.13(7)	$2.38(4) \times 10^{-5}$
9000 rpm	3.494(1)	$7.07(3) \times 10^{-3}$	63.62(1)	$2.40(2) \times 10^{-6}$

Table 2 SANS fits for the real-time VFD-SANS data at increasing VFD speeds, collected at ORNL using an uncoated quartz tube. The data were fitted with a summed power law + Lorentzian peak model. The peak HWHM indicates the width of the peak. The *d*-spacing was calculated from the peak position determined by the Lorentzian peak model, using the equation $d = 2\pi/q$, where q is the scattering vector. The ratio of the power scale to the peak scale indicates how much of the POPC is held in large structures like vesicles or liposomes *versus* the amount of POPC in multilamellar structures. Smaller ratios mean more POPC is in multilamellar structures. The digit in parentheses is the error in the last significant figure, and was calculated with either error propagation or from the SANS fit

Real-time VFD speed	(−) Power	Peak HWHM	*d*-spacing (Å)	Power scale/peak scale ratio
3800 rpm	3.337(8)	$9.0(5) \times 10^{-3}$	61.7(2)	$8.0(5) \times 10^{-6}$
4000 rpm	3.356(8)	$8.1(5) \times 10^{-3}$	61.5(2)	$6.8(4) \times 10^{-6}$
4500 rpm	3.388(7)	$8.3(4) \times 10^{-3}$	61.3(1)	$5.1(2) \times 10^{-6}$
5000 rpm	3.358(6)	$7.8(2) \times 10^{-3}$	61.41(9)	$5.7(2) \times 10^{-6}$
6000 rpm	3.36(1)	$7.2(5) \times 10^{-3}$	61.1(2)	$4.6(4) \times 10^{-6}$
7000 rpm	3.35(2)	$8.4(7) \times 10^{-3}$	60.9(3)	$4.9(5) \times 10^{-6}$
8000 rpm	3.36(1)	$7.9(6) \times 10^{-3}$	60.7(3)	$4.8(5) \times 10^{-6}$
9000 rpm	3.36(1)	$7.8(6) \times 10^{-3}$	61.0(2)	$4.7(4) \times 10^{-6}$

Although the multilamellar structures appear to become slightly thinner and less uniform once subjected to shear, these changes are small, and there appears to be no further changes with increasing levels of shear in the case of the thickness of the multilamellar structure. Interestingly, these effects occur once the system is sheared at 3800 rpm and hold reasonably constant up through 6000 rpm. At 7000 rpm, there is an odd break in the trends that do not recover as the shear increases further. Based on the model of the fluid flow in the VFD,[25,26] change in rotational speed in water is complicated by competing topological fluid flow from the Coriolis effect from the hemispherical base of the tube and the onset of double helical flow associated with Faraday waves for the oscillating thin film of liquid, Fig. 1. It is therefore not surprising that there is a region where there is a break in trend, where there is potentially transitioning from one dominant fluid flow to another.

The POPC system sheared in the uncoated quartz tube at ORNL (Table 2) responded differently from the system in the coated tube (Table 1). The largest difference is in the *d*-spacing, which is consistently about 3 Å shorter than that of the POPC in the coated tube. This could be due to slight differences in the ambient temperatures of ORNL and ANSTO when the respective data were collected. The *d*-spacing also gradually decreased as the shear speed increased, showing that the multilamellar layers tended to become thinner at higher shear levels. The peak also appears to narrow slightly as shear is applied, in the uncoated tube, indicating that the multilamellar layers become more uniform at higher shear levels. Additionally, the slope of the low-q decay is 3.34 upon onset of shear at 3800 rpm, and remained at approximately 3.35 as the shear increased, showing that the shear did not strongly affect the surface smoothness of the large liposomes. Finally, the power scale : peak scale ratio trends downwards as the shear increased, suggesting that either the concentration of POPC in the multilamellar structures increased with shear or the concentration of POPC making up the large liposomes decreased. These trends are all opposite from the response when sheared in the hydrophobically coated tube, except for the shear effects on the *d*-spacing, where it merely held constant as the shear became more intense. Interestingly, all trends, regardless of whether the VFD tube's inner surface was coated, were no longer maintained once the shear speed reached 7000 rpm. In particular, the scale ratio trend for the system studied with the uncoated tube appeared to reach a constant as the shear speed increased sufficiently. The break in trend at 7000 rpm is most likely associated with the changing dimensions of the high shear topological fluid flows in the VFD for increasing rotational speed, with spinning top flow increasing in diameter whereas double helical flow decreases in diameter, in a stepped fashion.[25]

With regards to the post-shear systems from the coated VFD tube (Table 3), there were no obvious correlations between the speed at which the system was sheared and the extent of lasting changes. In other words, higher shear speeds did not cause larger changes in the various aspects of the liposome structures,

Table 3 SANS fitting results to the post-shear data sets, collected at ANSTO using a quartz tube with a hydrophobic coating on the inner surface. The 0 rpm/unsheared sample was not sheared so any changes in structure due to shear in the VFD could be identified. The data were fitted with a summed power law + Lorentzian peak model. The peak HWHM indicates the width of the peak. The *d*-spacing was calculated from the peak position determined by the Lorentzian peak model, using the equation $d = 2\pi/q$, where q is the scattering vector. The ratio of the power scale to the peak scale indicates how much of the POPC is held in large structures like vesicles or liposomes *versus* the amount of POPC in multilamellar structures. Smaller ratios mean more POPC is in multilamellar structures. The digit in parentheses is the error in the last significant figure, and was calculated with either error propagation or from the SANS fit

VFD speed, post treatment	(−) Power	Peak HWHM	*d*-spacing (Å)	Power scale/peak scale ratio
0 rpm (unsheared)	3.367(2)	$8.4(1) \times 10^{-3}$	64.39(5)	$1.85(2) \times 10^{-5}$
3000 rpm	2.986(2)	$8.2(2) \times 10^{-3}$	64.6(1)	$1.70(4) \times 10^{-4}$
3800 rpm	2.914(2)	$8.2(4) \times 10^{-3}$	64.8(2)	$3.2(1) \times 10^{-4}$
4000 rpm	3.125(2)	$9.0(3) \times 10^{-3}$	64.8(1)	$8.2(2) \times 10^{-5}$
4500 rpm	2.842(2)	$7.4(5) \times 10^{-3}$	65.1(2)	$5.1(3) \times 10^{-4}$
5000 rpm	2.996(2)	$8.1(3) \times 10^{-3}$	64.8(2)	$1.95(6) \times 10^{-4}$
6000 rpm	2.731(2)	$6.4(4) \times 10^{-3}$	64.3(2)	$8.3(3) \times 10^{-4}$
7000 rpm	3.034(2)	$8.3(3) \times 10^{-3}$	65.0(1)	$1.48(4) \times 10^{-4}$
8000 rpm	2.707(2)	$6.0(5) \times 10^{-3}$	64.5(2)	$1.25(7) \times 10^{-3}$
9000 rpm	2.987(2)	$8.0(3) \times 10^{-3}$	64.7(2)	$2.21(7) \times 10^{-4}$

and the Coriolis force and Faraday wave fluid flows did not have significant effects on the structures This is consistent with these flows being involved in an equilibrium of assembled and disassembled POPC molecules which is not further perturbed for higher rotational speeds. The *d*-spacing stayed within 1 Å of the unsheared value, so the thickness of the multilamellar layers did not experience any lasting changes. The post-shear effects on the remaining three parameters (peak HWHM, power, and power scale : peak scale ratio) appear to be independent of shear speed, as they alternately increase and decrease as the speed increases. The slope of the low-q decay experienced a large decrease of 0.4–0.7 after shear compared to the unsheared system, indicating that there were fewer large liposomes contributing to the low-q signal. Despite this, the power scale : peak scale ratio was 1–2 orders of magnitude greater than it was before any shearing took place, indicating that there was a much higher concentration of POPC in the large liposomes or vesicles than there was in the multilamellar structures after shear. This significant change in the ratio is consistent with the observation of sludge on the surface of the samples 24 hours after shearing, coupled with an order of magnitude drop in the overall scattering intensity as well as in the intensity of the peak. The large drop in the overall scattering intensity means that the total concentration of POPC in the system decreased, while the less intense peak means that there were specifically fewer multilamellar structures in the system. Combined, these changes in the scattering data mean that all levels of shear greatly and preferentially affected the multilamellar liposomes, possibly by breaking them down or by forming a new multilamellar structure, causing the POPC within them to precipitate to form a sludge on the surface. Thus, the increase in power scale : peak scale ratio occurs due to the multilamellar structures suffering more significant damage from experiencing shear than the large liposomes or uni-lamellar vesicles.

The differences in the final geometry, structural thickness, and *d*-spacing as a function of shear may be due to the effects of the spinning top Coriolis force and double helical flow Faraday wave eddies, Fig. 1, that were present while the sample was being sheared. *In situ* SANS provides an insight into the formation of liposomes through this simple VFD processing technique. The high shear in the VFD produces higher curvature in the liposomal bilayer which distorts into transient ellipsoidal species and down to particles with a limiting number of POPC molecules. A fundamental understanding is achieved in the self-assembly and dis-assembly of liposomes which are fabricated through this high shear microfluidic platform.

Fluorophore labelling of the liposomes and their exchange was studied through this processing technique. This gives insights into the encapsulation of different bio-active molecules as well as the behaviour of the liposomes under shear stress in the VFD. Two different fluorophore-labelled liposomes were prepared initially by processing unlabelled liposomes under the same optimized conditions as above with a phospholipid suspension of 50 μg mL^{-1} in Milli-Q water. These were processed through a VFD at an optimised speed of 9000 rpm, under continuous flow at 0.1 mL min^{-1} flow-rate, θ +45° tilt angle in a hydrophobic tube, with the liposomes isolated through ultracentrifugation at 113 000*g* and then redispersed in PBS. The fluorophore lipid (1%) was added to this population and processed through VFD at lower rotational speed of 5000 rpm and the solution then characterized using DLS, measuring the size of generated fluorophore liposomes. The size of fluorophore labelled liposomes incorporating NBD-PE dye did not show any significant change relative to the size of the liposomes prepared for VFD processed POPC (un-labelled liposomes). Similarly, a comparison made between the size of POPC (unlabelled liposomes) and fluorophore labelled liposomes using Rh-PE dye did not show any significant change in the size of the liposomes.

Mo *et al.* reported that the lamellar thickness of a phospholipid bilayer mimic was approximately 5 nm. The results from the AFM height profile, Fig. 3, in the present study indicate that the formed liposomes are uni-lamellar.[30] In addition, the results show that the diameter of the deflated collapsed vesicles is about 15 nm; this is consistent with vesicles generated using a similar thin film process with a uni-lamellar or two bilayers

before collapsing.[30] The height of NBD-PE formed fluorophore labelled liposomes and Rh-PE fluorophore labelled liposomes are shown in Fig. 5. These observations indicate that there is no change in the uni-lamellar nature of the liposomes after adding a fluorophore labelled phospholipid. Given that POPC disassembles in the VFD, as established using *in situ* SANS, it is expected that labelled liposomes will be similarly disassembled and reassembled *in situ* when two different labeled liposomes are present. They are then expected to rearrange into liposomes with an equal mixture of the two fluorophore labeled phospholipid molecules, *i.e.* there is re-organization into liposomes post VFD processing. DLS revealed a particle size distribution around 180 nm for the mixed labelled liposomes, compared with the same size for Rh-PE labelled liposomes, and a broad size distribution around 250 nm for NBD labelled liposomes, Fig. 5. This reassembly of NBD-PE with POPC liposomes resulted in probe dilution (lipid-dye mixing) and an increase in distance between NBD-PE molecules in spreading throughout the POPC liposome, resulting in a reduced measurable emission intensity. Conventionally this has only

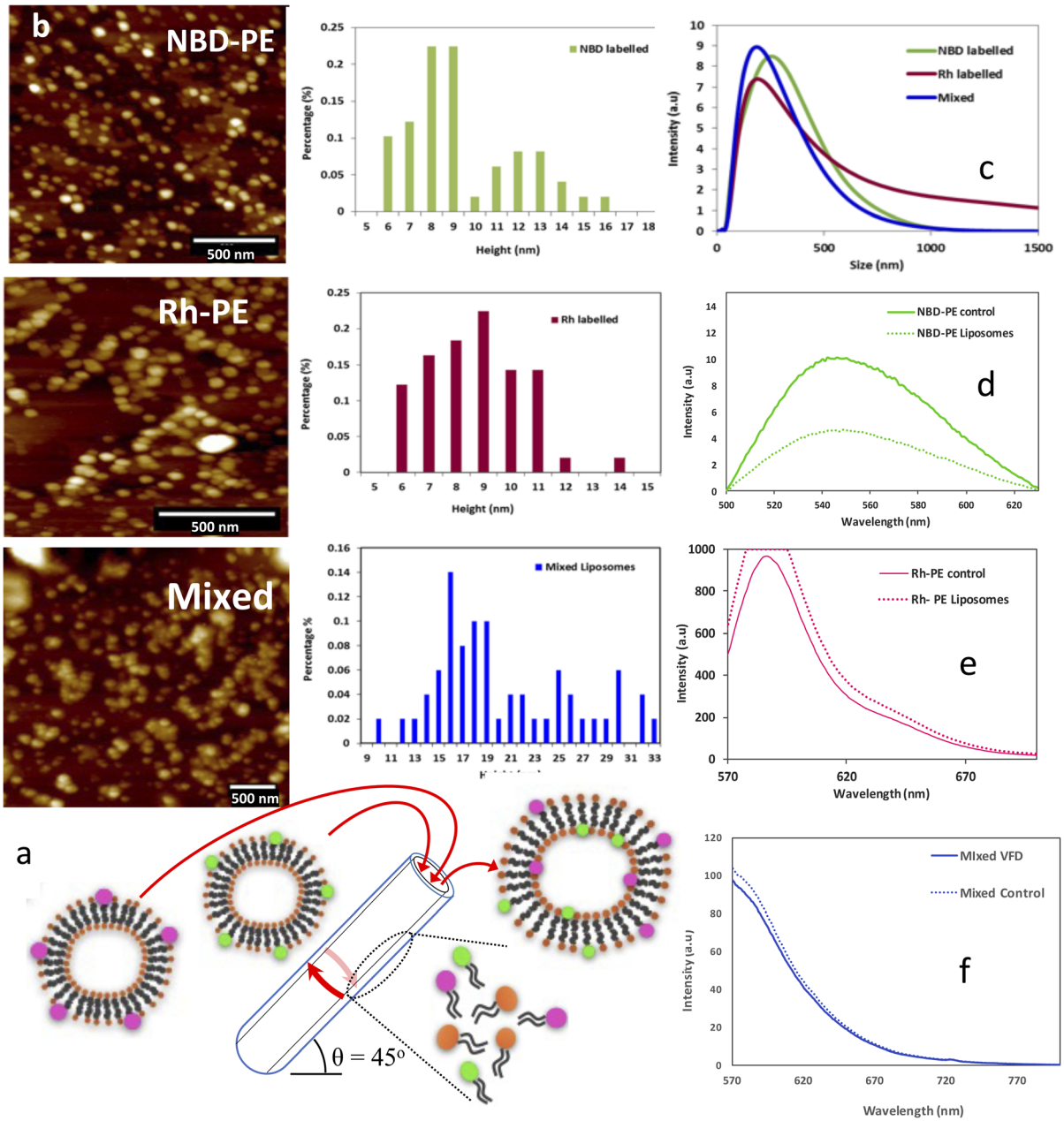

Fig. 5 (a) Schematic for VFD NBD-PE liposomes and VFD Rh-PE liposomes and mixed fluorophore labelled liposomes processed through a VFD at given conditions of ω 5000 rpm, 0.1% of fluorophore dye, confined mode, 1 mL of solution at θ +45° in a 20 mm (O.D.) VFD tube. (b) AFM images and height distribution profile for VFD processed fluorophore labelled liposomes and mixed fluorophore VFD liposomes. (c) DLS size distribution for VFD NBD-PE liposomes and VFD Rh-PE labelled liposomes and mixed fluorophore VFD liposomes. (d) Fluorescence spectrum for the VFD NBD-PE liposomes, (e) VFD Rh-PE fluorophore labelled liposomes and (f) VFD mixed liposomes.

been observed through a membrane fusion process.[34] In the present study, with the disassembly and reassembly of liposomes, a similar reduced emission intensity was encountered, although the formation of the mixed liposomes is not a fusion process, but rather involving disassemble and reassembly. For the Rh-PE fluorophore, there is an increase in the emission intensity. When both the labelled fluorophore liposomes were mixed together (1 mL of each solution) and processed in the VFD at 5000 rpm, compared to the control solution with no VFD processing, there was a decrease in the emission intensity. This clearly establishes that there was disassembly and reassembly such that there is a mixture of fluorophores in the liposomes. Processing in the VFD causes the quenching of the donor molecule in proximity and reduces the overall emission intensity.

Experimental

Materials

1-Palmitoyl-2-oleoyl-*sn*-glycerol-3-phosphocholine (POPC) was purchased from Sapphire Bioscience (NSW, Australia), fluorophore lipids: Rh-PE 1,2-dipalmitoyl-*sn*-glycero-3-phosphoethanolamine-*N*-(lissamine rhodamine B sulfonyl) (ammonium salt), and NBD-PE (1-oleoyl-2-hydroxy-*sn*-glycero-3-phosphoethanolamine-*N*-[tetra-(ethylene glycol)]-*N*′-(7-nitro-2-1,3benzoxadiazol-4-yl)) (ammonium salt) were obtained from Avanti Polar Lipids. Milli-Q water was utilised for all the experiments.

Liposome assembly

A phospholipid suspension of 50 g mL^{-1} in Milli-Q water was processed through VFD at an optimised speed of 9000 rpm, 0.1 mL min^{-1} flow-rate, 45° tilt angle in continuous flow in a hydrophobic tube.

Labelling liposomes with fluorophore lipids

Liposomes fabricated by VFD were isolated through ultracentrifugation at 113 000*g* and redispersed in phosphate-buffered saline (PBS); 1% of the fluorophore lipid was added to this population and processed through VFD at the lower rotational speed of 5000 rpm.

Nanoparticle tracking analysis (NTA)

The size distributions of the liposomes were analyzed using a Nano Sight LM10 instrument (Malvern instruments Ltd, Worcestershire, UK) equipped with NTA software version 2.3. The particle suspensions were diluted with PBS to a concentration of ~108 particles per mL for analysis. Data were taken in triplicate 60 second videos to get a standard error for the data.

Scanning electron microscopy (SEM)

Samples were characterised using an Inspect FEI F50 SEM (PS216) instrument. The spot size was 3.0, voltage was 5.0 kV and magnification was 50 000. Sample preparation for SEM was as follows: 20 μL of as-prepared sample was drop casted on a silicon wafer and air dried overnight, followed by platinum sputter coating of a ~2 nm thick layer for subsequent SEM imaging.

Atomic force microscopy (AFM)

Samples were analyzed with atomic force microscope (AFM) (Nanoscope V, Multimode 2 SPM). Images were acquired using silicon probes in tapping mode in air with Scanner "E" from 500 nm 3 μm scan sizes. The sample preparation for AFM was as follows: 20 μL of 1 : 100 diluted sample was drop casted onto silicon wafer and air dried overnight whereupon the samples were washed 3 times with Milli-Q water prior to recording the AFM images.

Transmission electron microscopy (TEM)

TEM was conducted on a FEI Titan Themis 80–200 instrument. The sample preparation was as follows: 20 μL of sample was fixed on the carbon grids and left to air dry for 1 h, with the excess sample removed using blotting paper, followed by staining using 2 g/100 mL uranyl acetate solution. TEM images were then taken under the voltage of 100 keV.

SANS sample preparation

Solutions of 0.1 wt% POPC phospholipid solutions were prepared in D_2O. 2 mL of solution were added into a quartz VFD tube OD 20 mm with an inner hydrophobic surface (ANSTO) in confined mode at lower speed of 3800, 4000, 4500 and 5000 rpm, while 1 mL of solution was added for higher speeds such as 7000, 8000 and 9000 rpm. This was repeated with another quartz VFD tube of the same dimensions with no coating on the inner surface (ORNL). All the VFD samples were collected and characterized post-VFD with conventional SANS. As-received sample without any processing was also characterized with SANS.

SANS data acquisition and analysis

All the SANS experiments were carried out on Bilby (ANSTO, Lucas Heights, Australia) and on Bio-SANS (ORNL, Oak Ridge, TN, USA). The VFD microfluidic device was mounted on the *xyz* goniometer stage with an aluminum shield containing a silicon window through which the neutron beam could pass. The stage was adjusted with respect to the neutron beam such that the beam-centre was placed 3 cm from above the base of the tube.

Data were collected on the Bilby instrument[35] at ANSTO using the VFD tube with a hydrophobic coating on the inner surface. A time-of-flight configuration was used, utilizing neutron wavelengths between λ = 2–20 Å, and a wavelength resolution of $\frac{\Delta\lambda}{\lambda} = 0.12$. Sample-detector distances (SDD) were set to 3.5 m, 4.5 m and 7.0 m to achieve the full q-range of 0.00216 $Å^{-1} < q < 0.36309$ $Å^{-1}$, where the scattering vector $q = (4\pi/\lambda)\sin(\theta/2)$, λ is the neutron wavelength, and θ is the scattering angle. The measurement was performed at room temperature ~20 °C, without active control.

For the data collected on Bio-SANS at ORNL using the uncoated VFD tube, all data was collected using a neutron beam wavelength $\lambda = 6$ Å, with a spread of $\frac{\Delta\lambda}{\lambda} = 0.15$. The data were collected simultaneously with the main detector SDD of 15.5 m for low-q, and the high-angle detector SDD of 1.14 m for the high-q data.[35] Acquisition times were up to 30 min. No neutron guides were used, so the source-to-sample distance was 17.68 m. When the high-q and low-q data were combined, these settings yielded a complete q-range of 0.003–0.85 $Å^{-1}$. The experiment was performed at room temperature ~21 °C, without active control.

All the datasets were corrected for solvent scattering using D_2O blanks measured at the same speed, empty quartz tube scattering, and detector sensitivity. The data were placed on an absolute scale using attenuated direct beam transmission measurements. Finally, the reduced 2D data were radially averaged to yield the 1D scattering curve. Mantid software[36] for the ANSTO data and drt-SANS software for the ORNL data[37] were employed for data reduction while the NIST macros for Igor Pro (Wavemetrics, Portland, OR, USA)[38] were used for data fitting.

Fluorescence spectroscopy measurements

All the fluorescence measurements were carried out with Cary Eclipse Fluorescent Spectrophotometer, Agilent technologies using quartz cells of path-length 10 mm. Both excitation and emission band slits were fixed at 10 nm and the scan rate was selected at 1800 nm min^{-1}. The excitation wavelength was selected at 460 nm for the NBD-PE fluorophore while emission spectra were collected in the range of 480–600 nm. The excitation wavelength for Rh-PE was selected as 560 nm and emission was collected from 570–650 nm.

Conclusions

A straightforward process has been developed for fabricating liposomes under continuous flow processing in a high shear vortex fluidic device (VFD). The optimum processing parameters were determined for the concentration of the phospholipid, the rotational speed of the +45° inclined tube in the thin film microfluidic platform, and flow rate. *In situ* SANS was used to determine the morphology of the species present under shear in the VFD using a quartz tube with a hydrophobic coating on the inner surface, and another quartz tube with no coating. Large liposomes and multilamellar structures coexisted in the system regardless of the tube used, but the trends observed as a function of shear speed using one tube was opposite the trends observed with the other tube. After the system was sheared in the hydrophobically coated tube, no trends could be observed as a function of shear speed. However, there was a large drop in the overall concentration of POPC in the system at each level of shear caused by the formation of sludge on the surface, with the shear primarily affecting the multilamellar structures and also the large liposomes to a lesser extent. Fluorophore tags can be introduced into the liposomes without disturbing the final geometry (no-VFD processing) and, when two types of liposomes bearing 1% fluorophores are mixed in the VFD, the resulting liposomes have equal populations of the two fluorophores, in accordance with the mechanistic findings from SANS. This approach represents a paradigm shift in fabricating liposomes with the ability to have control over their disassembly and re-organization without the need for downstream processing. The induced mechanical energy in the VFD generates *in situ* sub-micelle species which assemble into ~110 nm diameter liposomes, establishing them as the thermodynamically stable structure from bottom-up self-assembly. This diameter is similar to that of exosomes, suggesting that their diameter is similarly governed, although here there are potentially structural influences from membrane proteins.

Author contributions

N. J. and T. A. carried out the synthesis of the liposomes including labelling studies; N. J., T. A., A. H. M. A. and M. J. carried out characterisation studies (SANS excepted); M. M., D. P. H., E. C., H. K., E. P. G., A. W., S. Q., L. H. and H. K. collected the SANS data, with modelling undertaken by M. M, H. K. and A. W.; C. L. R. designed the microfluidic platform, coordinated the research and the writing of the manuscript. All authors contributed to writing and editing the manuscript.

Conflicts of interest

There are no conflicts to declare.

Acknowledgements

The authors acknowledge support of this work by the Australian Research Council (DP200101105 and DP200101106) for funding support, Australian Nuclear Science & Technology organization ANSTO for the beamtime (proposals 7015,7402 and 13375) to carry out the experiments and their guidance and support throughout this project. The authors acknowledge the Australian Microscopy and Microanalysis Research Facility (AMMRF) and Australian National Fabrication Facility (AMMRF) for SEM, dual target sputter coater and AFM imaging. A portion of this research used resources at the High Flux Isotope Reactor, a DOE Office of Science User Facility operated by the Oak Ridge National Laboratory. Authors also acknowledge Adelaide Microscopy at The University of Adelaide (UoA), South Australia for TEM imaging and Flinders Centre for Innovation in Cancer (FCIC), South Australia for the guidance and support throughout this project. Funding for Bio-SANS is provided by the Office of Biological & Environmental Research in the U.S. Department of Energy's Office of Science.

References

1 T. Allen and P. Cullis, *Adv. Drug Delivery Rev.*, 2013, **65**, 36–48.
2 M. Salim, H. Minamikawa, A. Sugimura and R. Hashim, *MedChemComm*, 2014, **5**, 1602–1618.
3 X. Luan, *et al.*, *Acta Pharmacol. Sin.*, 2014, **38**, 754–763.
4 Y. Sato, *et al.*, *Sci. Rep.*, 2016, **6**, 21933.

5 D. Carugo, E. Bottaro, J. Owen, E. Stride and C. Nastruzzi, *Sci. Rep.*, 2106, **6**, 25876.
6 S. Pande, *Artif. Cells, Nanomed., Biotechnol.*, 2023, **51**, 428–440.
7 H. Shum, D. Lee, I. Yoon, T. Kodger and D. Weitz, *Langmuir*, 2008, **24**, 7651–7653.
8 Q. Xu, *et al.*, *Small*, 2009, **5**, 1575–1581.
9 A. Jahn, W. Vreeland, M. Gaitan and L. Locascio, *J. Am. Chem. Soc.*, 2004, **126**, 2674–2675.
10 S. Matosevic and B. Paegel, *J. Am. Chem. Soc.*, 2011, **133**, 2798–2800.
11 H. Shan, *et al.*, *Small*, 2023, **19**, 2205498.
12 V. D. Francesco, *et al.*, *Biomed. Microdevices*, 2023, **25**, 29.
13 J. Britton, K. Stubbs, G. Weiss and C. L. Raston, *Chem.–Eur. J.*, 2017, **23**, 13270–13278.
14 J. Britton, L. Meneghini, C. L. Raston and G. A. Weiss, *Angew. Chem.*, 2016, **128**, 11559–11563.
15 J. Britton and C. L. Raston, *Chem. Soc. Rev.*, 2017, **46**, 1250–1271.
16 K. Vimalanathan, *et al.*, *Angew. Chem.*, 2016, **129**, 8518–8521.
17 T. Yuan, *et al.*, *ChemBioChem*, 2015, **16**, 393–396.
18 J. Phillips, *et al.*, *ACS Appl. Bio Mater.*, 2018, **2**, 488–494.
19 G. Oksdath-Mansilla, R. Kucera, J. Chalker and C. L. Raston, *Chem. Commun.*, 2021, **57**, 659–662.
20 J. Tavakoli, C. L. Raston and Y. Tang, *Molecules*, 2020, **25**, 3445.
21 S. He, N. Joseph, X. Luo and C. L. Raston, *Lebensm.-Wiss. Technol.*, 2019, **103**, 88–93.
22 X. Cao, *et al.*, *Food Funct.*, 2021, **12**, 1087–1096.
23 X. Luo, *et al.*, *ACS Appl. Mater. Interfaces*, 2018, **10**, 27224–27232.
24 X. Luo, *et al.*, *ACS Appl. Mater. Interfaces*, 2020, **12**, 51999–52007.
25 T. M. D. Alharbi, *et al.*, *Nanoscale Adv.*, 2021, **3**, 3064–3075.
26 M. Jellicoe, *et al.*, *Chem. Sci.*, 2020, **13**, 3375–3385.
27 S. He, *et al.*, *NPJ Sci. Food*, 2020, 12.
28 A. Zaccone, *et al.*, *Phys. Chem. Rev. E*, 2009, **80**, 052404.
29 B. O. Conchuir and A. Zaccone, *Phys. Chem. Rev. E*, 2013, **87**, 032310.
30 J. Mo, *et al.*, *Sci. Rep.*, 2015, **5**, 10414.
31 K. Vimalanathan, *et al.*, *Nanoscale Adv.*, 2022, **4**, 3121–3130.
32 W. T. Heller, *et al.*, *J. Appl. Crystallogr.*, 2014, **47**, 1238–1246.
33 B. Hammouda, *Probing Nanoscale Structures, the SANS Toolbox*, National Institute of Science and Technology Center for Neutron Research, 2016.
34 Y. Zeng, *et al.*, *Small*, 2023, **19**, 2301133.
35 A. Sokolova, *et al*, *J. Appl. Crystallogr.*, 2019, **52**, 1–12.
36 O. Arnold, *et al.*, *Nucl. Instrum. Methods Phys. Res.*, 2014, **764**, 156–166.
37 W. T. Heller, *et al.*, *SoftwareX*, 2022, **19**, 101101.
38 S. Kline, Reduction and analysis of SANS and USANS data using IGOR Pro, *J. Appl. Crystallogr.*, 2006, **39**, 895–900.